

Selective Induction of Optical Magnetism

Uttam Manna,^{†,§} Jung-Hoon Lee,^{‡,§} Tian-Song Deng,^{‡,§} John Parker,^{†,§,§} Nolan Shepherd,^{†,‡} Yossi Weizmann,[‡] and Norbert F. Scherer^{*,†,‡}

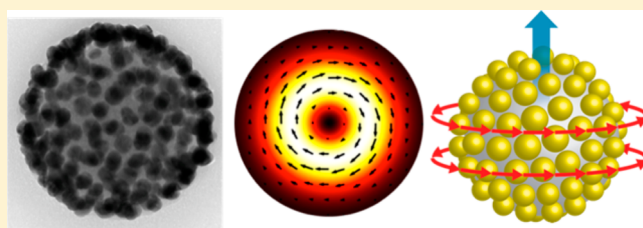
[†]The James Franck Institute, [‡]Department of Chemistry, [§]Department of Physics, University of Chicago, Chicago, Illinois 60637, United States

Supporting Information

ABSTRACT: An extension of the Maxwell–Faraday law of electromagnetic induction to optical frequencies requires spatially appropriate materials and optical beams to create resonances and excitations with curl. Here we employ cylindrical vector beams with azimuthal polarization to create electric fields that *selectively drive magnetic responses* in dielectric core–metal nanoparticle “satellite” nanostructures. These optical frequency magnetic resonances are induced in materials that do not possess spin or orbital angular momentum.

Multipole expansion analysis of the scattered fields obtained from electrodynamics simulations show that the excitation with azimuthally polarized beams selectively enhances magnetic vs electric dipole resonances by nearly 100-fold in experiments. Multipolar resonances (e.g., quadrupole and octupole) are enhanced 5-fold by focused azimuthally versus linearly polarized beams. We also selectively excite electric multipolar resonances in the same identical nanostructures with radially polarized light. This work opens new opportunities for spectroscopic investigation and control of “dark modes”, Fano resonances, and magnetic modes in nanomaterials and engineered metamaterials.

KEYWORDS: Optical magnetism, cylindrical vector beams, multipolar resonances, FDTD simulations, plasmonic nanocluster, meta-atom



It is well-known that one can create a magnetic field by passing a DC or AC electric current through a coil of a conductor (i.e., a wire); a phenomenon described by the Maxwell–Faraday’s law of electromagnetic induction.¹ Nuclear magnetic resonance and electron spin resonance (NMR and ESR) spectroscopies involve the interaction of a spin with a magnetic field. Mathematically, these phenomena can be understood as the curl of the electric field (i.e., from the current or spin) producing a (time varying) magnetic field or the inverse process. Thus, it should be possible to induce a magnetic response in materials, either through the design of the structure and/or by employing an electric field with instantaneous curl, by creating an instantaneous “circulating” current.

Magnetic resonance is conventionally associated with the absorption and emission of electromagnetic radiation in systems that possess magnetic moments and (spin or orbital) angular momentum. NMR and ESR are described by an interaction of the magnetic moments of charged particles with spin angular momentum (nuclear or electron, respectively) with an external magnetic field and typically occur at radio or microwave frequencies.^{2–5} Magnetic dipole transitions in atomic systems, which can occur at optical frequencies, involve changes in the total angular momentum (spin and angular). However, the magnetic dipole interactions with applied electromagnetic fields are orders of magnitude weaker than electric dipole transitions,⁶ with the exception of rare earth ions such as Eu^{3+} that have naturally occurring magnetic resonances

with strengths comparable to electric resonances.⁷ Novotny and co-workers recently demonstrated selective excitation and enhancement of the magnetic dipole transition of Eu^{3+} using the spatially localized magnetic field associated with focused azimuthally polarized light.⁸

Nano-to-meso scale materials are known or can be designed to have magnetic dipole modes even though they do not intrinsically possess spin or orbital angular momentum: for example, Mie-type dielectric resonators with a high refractive index such as silicon⁹ or Mie scattering from noble metal nanoparticles (with diameter ~ 100 nm or larger) exhibit multipolar scattering involving both electric and magnetic modes at optical frequencies that stem from retardation¹⁰ or can be induced using circularly polarized light. A simulation study with cylindrical vector beams (CVBs) indicated the potential to manipulate multipolar phenomena in multiparticle dielectric resonators and selectively excite “dark modes” in the dielectric resonators.¹¹ Electromagnetic meta- or “left-handed” materials, which do not occur in nature and must be constructed, have both negative permittivity (ϵ) and permeability (μ) in some range of frequencies.^{12–14} Achieving negative ϵ and μ is synonymous with having strong (and relatively sharp) electric and magnetic (dipolar) resonances,

Received: May 22, 2017

Revised: October 11, 2017

Published: November 7, 2017

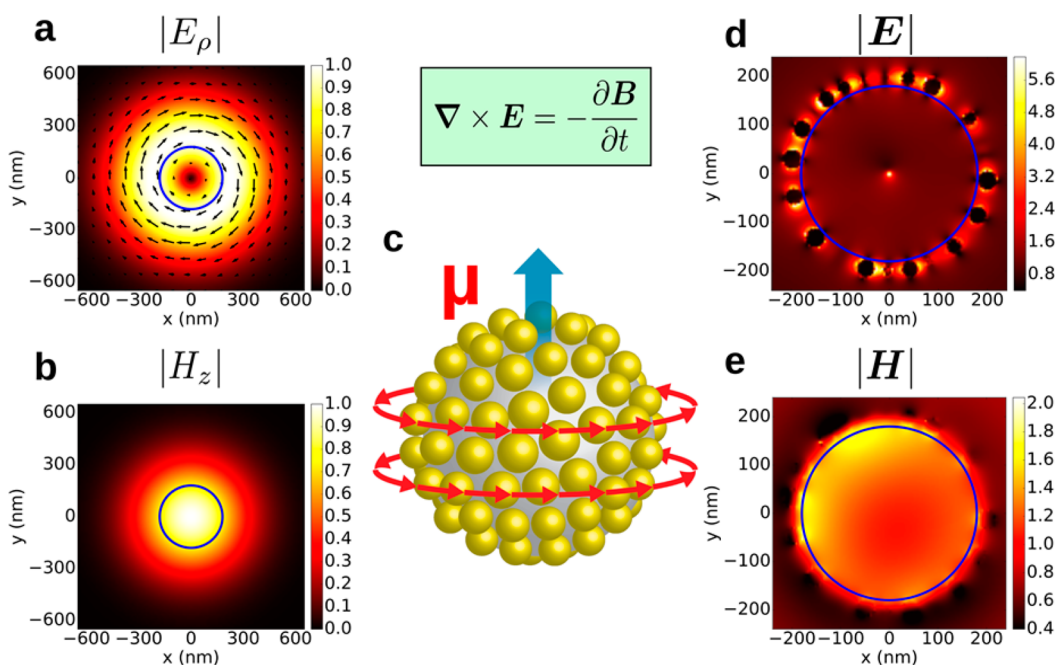


Figure 1. Azimuthally polarized vector beam and excitation of nanoclusters. (a) Simulation of the transverse component of the incident electric field ($|E_\rho|$) and (b) longitudinal component of the incident magnetic field ($|H_z|$) of an azimuthal beam focused with numerical aperture (NA) = 1.4. (c) Schematic of a core (SiO₂)–satellite (Ag) nanocluster and the manifestation of the Maxwell–Faraday equation at an instant in time with an azimuthal vector beam. The blue arrow that depicts the induced magnetic field is oriented along the z -axis, which is the beam propagation direction. (d) Electric field enhancement, $|E_{\text{scat}} + E_{\text{incl}}|/|E_{\text{incl}}|$, and (e) the magnetic field enhancement, $|H_{\text{scat}} + H_{\text{incl}}|/|H_{\text{incl}}|$. (d, e) are the results of FDTD simulations of the core–satellite cluster shown in panel c with an incident field at 700 nm wavelength. The blue circle represents the SiO₂ core with a diameter of 360 nm. The simulated Ag NPs are 43 nm in diameter. The inhomogeneities in the electric and magnetic field intensities arise due to the nonsymmetric packing and size distribution of the Ag nanoparticles that are created at the “equatorial” cross-section.

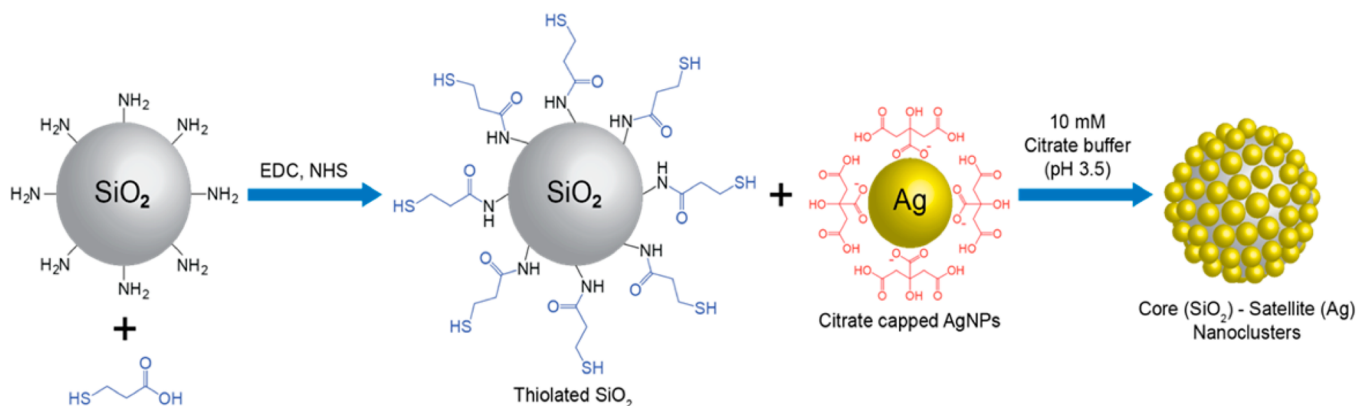
respectively. Spectral overlap of the electric and magnetic resonances, which would ideally be comparable in magnitude (cross-section), would yield a meta-material that is expected to have a negative refractive index at optical frequencies,^{15–18} exhibit unidirectional scattering,^{19,20} or Fano resonance.^{19,21}

In this paper we present an approach to selectively excite and measure magnetic or electric multipolar resonances in nano-to-meso scale materials, and analyze these resonances and their magnetic or electric nature via finite-difference time-domain (FDTD) calculations. The systems we study are mesoscale structures consisting of metal (Ag) nanoparticles that are covalently attached to the surface of a dielectric (SiO₂) core. These (dielectric-metal) core–satellite structures, termed nanoclusters or “meta-atoms”, are putative building blocks self-assembled into meta-materials and meta-fluids,^{22–24} because they are expected to have strong magnetic responses, with spatially isotropic properties scalable to macroscopically large samples.^{15,22–24} They rely on the plasmonic resonant feature of the metal nanoparticles and their electromagnetic coupling to create a circular “displacement” current.^{15–18}

As shown in Figure 1 (focused) azimuthally polarized light, a cylindrical vector beam (CVB),²⁵ that has an instantaneous curl of the electric field can excite an oscillating cylindrical current in space that efficiently induces an AC magnetic response in metal nanoparticle based systems. In fact, the vector beam spectroscopy that we demonstrate is a direct manifestation of the Maxwell–Faraday equation,¹ $\nabla \times \mathbf{E} = -\partial \mathbf{B} / \partial t$. Instead of the magnetic fields being created by induction due to circulating electric currents (i.e., electromagnets), here the electric field oscillates at subpetahertz frequencies (i.e., visible light). The induction arises from displacement currents created

by resonant excitation of electric dipoles in the nanoparticles that are, in turn, electro-dynamically coupled (from particle to particle) around the core–satellite cluster. Our FDTD calculations with multipole expansion analysis show that excitation with azimuthally polarized light selectively enhances magnetic vs electric dipole resonances by nearly 100-fold in experiments. Multipolar resonances (e.g., quadrupole and octupole) are enhanced 5-fold by focused azimuthal beams vs linearly polarized light. Moreover, we also measure spatially orthogonal (pure) electric multipolar resonances by excitation with radially polarized light.

Unfortunately, three-dimensional nanoclusters synthesized by nanochemistry suffer from inhomogeneities in nanoparticle size, shape, and in the arrangement and density of metal nanoparticles on the surface of a dielectric (or other) core, which cause variations in the spectral responses and hence of the permittivity and permeability of the nanocluster meta-atoms. As is now well-appreciated in single molecule science, these variations and heterogeneities cannot be uniquely ascertained from ensemble spectra. Thus, in addition to selectively exciting magnetic/electric modes in these nanoclusters, measuring the optical response of single nanoclusters is an essential aspect of material characterization. Therefore, we conduct our measurements with focused vector beams on single nanoclusters of varying size and nanoparticle surface density, characterize the same single nanoclusters by transmission electron microscopy (TEM), and conduct FDTD simulations for comparison. These correlated measurements and simulations give an appreciation for the heterogeneity of the magnetic and electric multipolar responses.

Scheme 1. Synthesis of Nanoclusters^a

^aSchematic representation of the assembly of core–satellite nanocluster (see Methods). Various sizes of SiO₂ particle cores and Ag nanoparticle satellites were used in the fabrication of core-satellite nano-clusters (meta-atoms).

Generation and Characterization of Cylindrical Vector Beams (CVBs). The state of polarization of scalar beams (e.g., linearly, elliptically, and circularly polarized light) does not depend on the spatial location over the beam cross-section; they have spatially homogeneous states of polarization. On the other hand, CVBs are solutions of Maxwell's equations that possess spatially varying polarization with cylindrical symmetry in both amplitude and phase.²⁵ Such beams can have (i) their electric field aligned in azimuthal orientations, while their magnetic field is radially directed with respect to the optical axis; or (ii) their magnetic field has azimuthal orientations while the electric field is radially polarized with respect to the optical axis or other more complex forms.^{25–29} These are respectively known as azimuthally and radially polarized CVBs. Figure S1a depicts an azimuthal CVB showing that these cylindrical beams change their handedness over each half of the optical cycle. Therefore, azimuthal CVBs have instantaneous curl, but no net angular momentum. The CVBs with azimuthal and radial polarization can be expressed as superpositions of orthogonally polarized Hermite–Gauss HG₀₁ and HG₁₀ modes^{27,29} as depicted in Figure S1a.

Both active and passive methods have been developed to generate CVBs.^{29–31} The vector beam generator that we reported in 2005³¹ and others are not achromatic. For the present experiments, we use a liquid-crystal (LC) based polarization converter (from ARCoOptix) that uses twisted nematic liquid crystals sandwiched between one uniform and one circularly rubbed alignment layer to generate azimuthally and radially polarized CVBs.³² See the Supporting Information (SI) for details of the setup and relevant characteristics of the azimuthal beam (Figure S1).

Focused Cylindrical Vector Beams and Nanocluster Excitation. It has been shown that focusing CVBs with a lens (objective) with a finite numerical aperture in the nonparaxial limit causes spatial separation of the electric and magnetic fields at the focus and leads to longitudinal polarization of the electric or magnetic field.^{27,33} The longitudinal (*z*)-component of the magnetic (electric) field dominates the transverse (ρ) component of the magnetic (electric) field in the focal region, whereas the electric (magnetic) field component is purely transverse for azimuthal (radial) polarized beams under very high-NA focusing.^{27,33} The distributions of the radial component of the electric field ($|E_{\rho}|$), and the longitudinal component of the magnetic field ($|H_z|$) are shown in Figures 1a

and 1b. Whereas Novotny and co-workers utilized the longitudinal component of magnetic field, $|H_z|$, of a focused azimuthally polarized beam to enhance an “inherent” magnetic dipole transition in Eu³⁺ ions embedded in a Y₂O₃ nanoparticle,⁸ our spectroscopic measurements emphasize the transverse component of the electric field, $|E_{\rho}|$. The focused azimuthally polarized beam excites the dipoles in the metal nanoparticle “satellites” and drives an instantaneous curl of their collective electronic excitation thus inducing a mesoscopic magnetic response in a core (SiO₂)–satellite (Ag) nanocluster. This is illustrated in Figure 1c; the azimuthally polarized (focused) electric field creates dipolar plasmon excitations of the Ag nanoparticles and hence an instantaneous displacement current among the equatorially coupled nanoparticles (Figure 1d). The instantaneous cylindrical displacement current is expected to induce a time varying magnetic field according to $\nabla \times \mathbf{E} = -\partial \mathbf{B} / \partial t$ that is directed along the poles of the nanoclusters as shown in Figure 1e.

Nanocluster Synthesis. We prepared self-assembled core (dielectric)–satellite (metal) nanoclusters by covalently attaching metal nanoparticles to the surface of a chemically functionalized dielectric core. Scheme 1 represents a facile synthetic strategy for core (SiO₂)–satellite (AgNPs) nanoclusters. Briefly, citrate-stabilized AgNPs with different diameters were synthesized by a method modified from the literature.³⁴ Silica particles functionalized with thiol groups were mixed with silver nanoparticles (AgNPs) and dispersed in a 10 mM citrate buffer (pH = 3.5). We tuned the electrostatic interactions to control the AgNPs density on the silica core surface—the more highly protonated citrate at low pH makes the AgNPs less repulsive to each other and allows more dense packing of AgNPs around the silica core via Ag–S dative bonding.³⁵ The resulting solution of nanoclusters is dispersed in deionized water for storage and further measurements (more details are given in Methods). The assembled structures were characterized via TEM and UV-vis-NIR spectroscopy. Figures 2a and e show TEM images of two typical nanoclusters with different core and satellite sizes. The ensemble UV-vis spectra and their associated TEM images for nanoclusters with various structural parameters are shown in Figure S2.

Measurement of Single Nanocluster Spectra. We measured the scattering spectra of individual core (SiO₂)–satellite (Ag) nanoclusters with different core and satellite sizes being illuminated with focused linearly, azimuthally, and

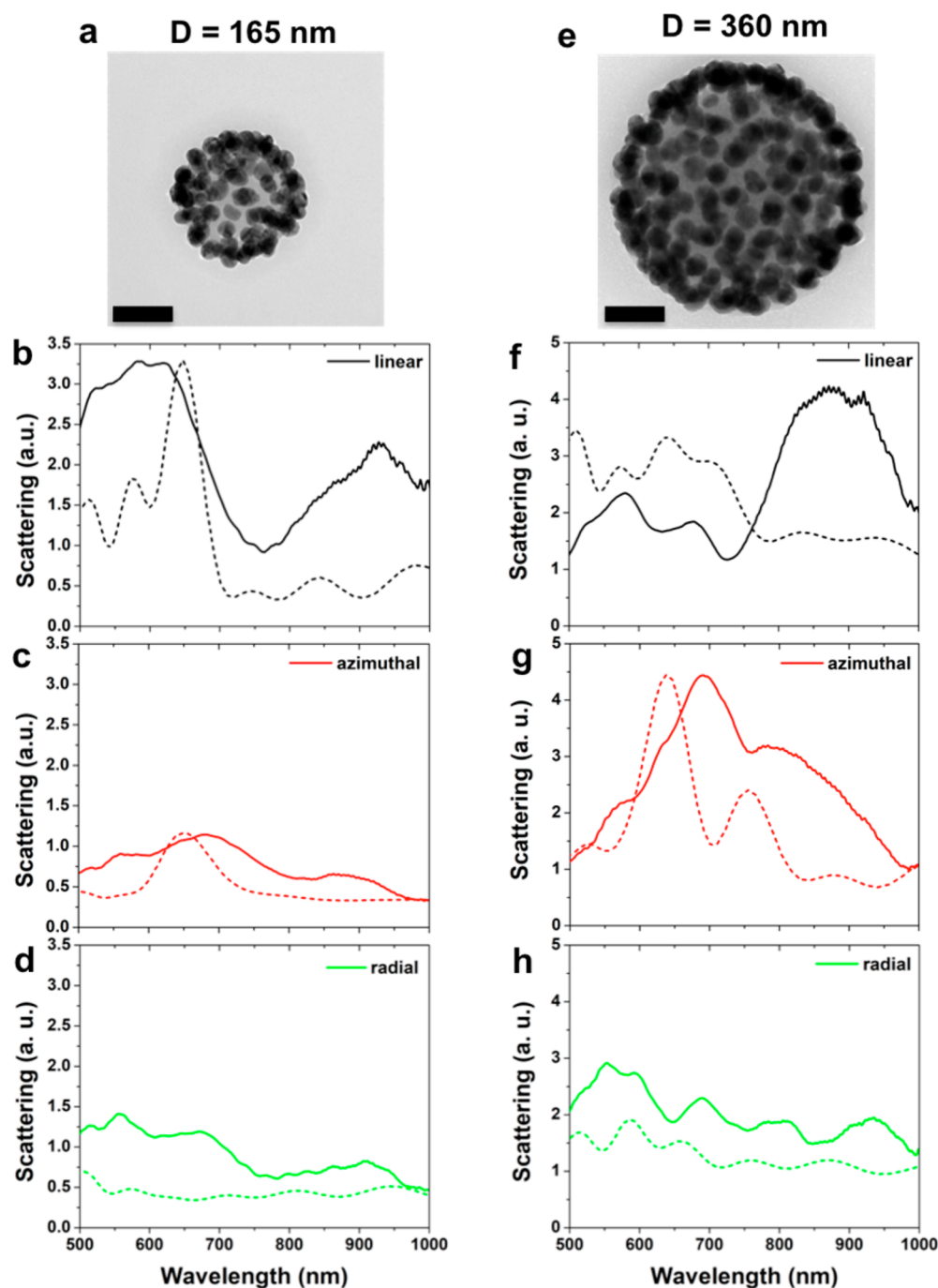


Figure 2. Optical backscattering measurements and simulations of single nanocluster spectra excited by cylindrical CVBs and linearly polarized light. (a–d) TEM image, experimental and simulated scattering spectra of a particular core–satellite nanocluster with core size of ~ 165 nm and AgNPs of ~ 30 nm in diameter. (e–h) TEM image, experimental and simulated scattering spectra of a particular core–satellite nanocluster with core size of 360 nm and AgNPs of ~ 43 nm in diameter. The scattering spectra were excited by linearly (black), azimuthally (red), and radially (green) polarized light, respectively. Scale bars in panels a and e are 100 nm. While the intensities of the simulated spectra are arbitrary units, all of the spectra can be compared with the scales shown. Similarly, the magnitudes of experimental spectra in b–d can be directly compared and those in f–h. Only the azimuthal spectra were adjusted to match experiment and simulation maximum values.

radially polarized light using the vector beam spectroscopy setup described in [Materials and Methods](#) and [Figure S1b](#). The sample was made by drop casting the nanocluster sample on a Formvar coated TEM finder grid that allowed facile correlation of TEM images and optical measurement ([Figure S3](#)). After taking TEM images, the grid was immersed in $n = 1.52$ index matching oil and sandwiched by two glass cover slides. Thus, the refractive index of the Formvar ($n = 1.50$) and glass slides

($n = 1.52$) is nearly perfectly matched so the reflection and scattering from the oil/Formvar interface is very weak. This is important since a significant reflection from the interface will interfere with the backscattered light from the nanocluster altering its spectrum.

[Figure 2](#) shows representative experimental backscattering spectra and TEM images for nanoclusters with two different core diameters: (i) Core diameter, $d_c \sim 165$ nm; satellite

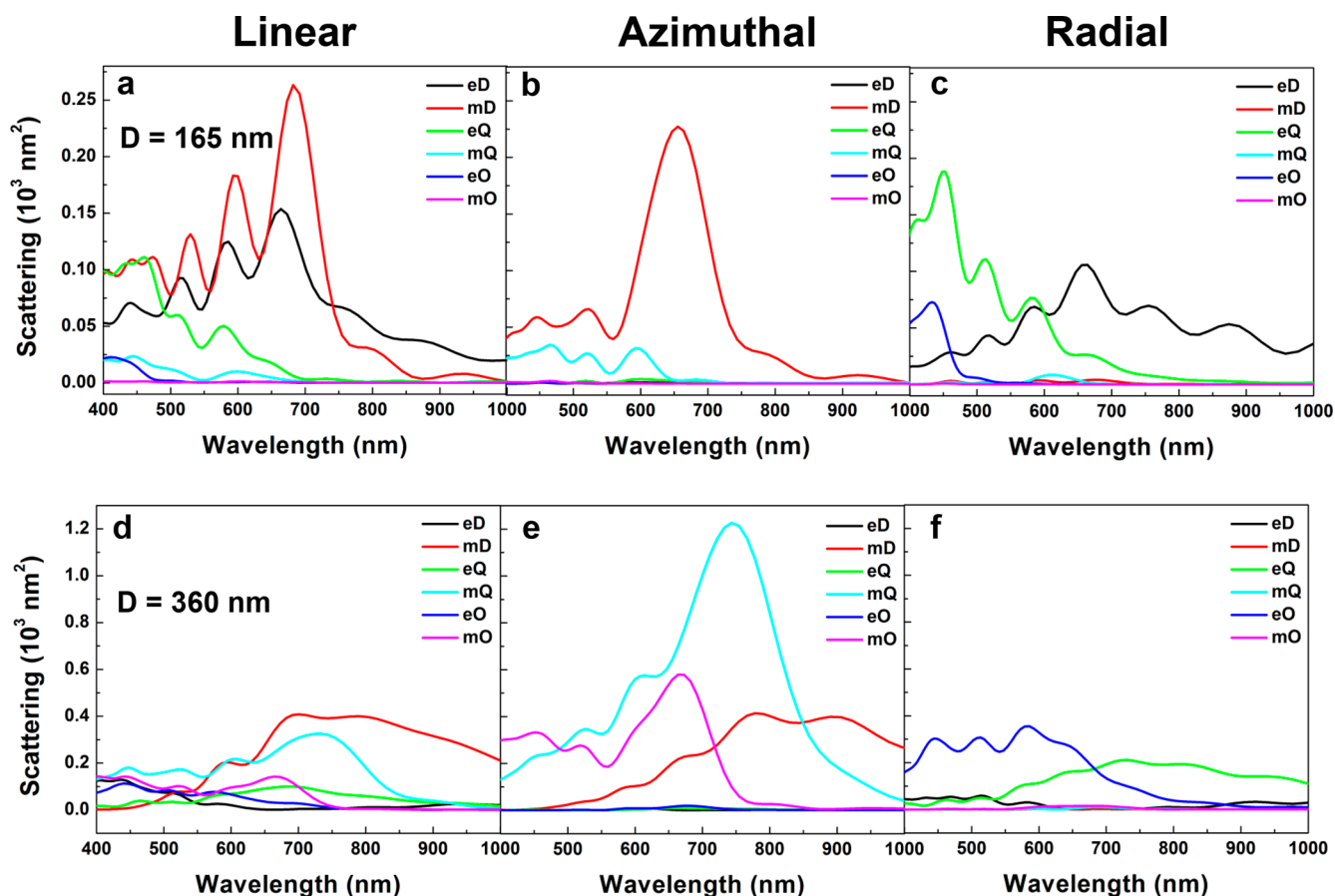


Figure 3. Expansion of the FDTD scattering amplitudes into electric and magnetic multipolar modes. (a–c) $D = 165$ nm and (d–f) $D = 360$ nm. Each simulated spectrum in Figure 2 is decomposed into the six lowest order multipolar modes: electric dipole (eD), magnetic dipole (mD), electric quadrupole (eQ), magnetic quadrupole (mQ), electric octupole (eO), and magnetic octupole (mO), respectively. The spectra excited by the azimuthal CVB are exclusively magnetic modes, whereas the spectra excited by the radial CVB are exclusively electric modes. Excitation with focused linearly polarized light gives both.

diameter, $d_s \sim 30$ nm with a standard deviation, $\sigma \sim 3$ nm; number of satellites, NoS ~ 80 (henceforth called NC_D165 nm, corresponds to Figure 2a–d); (ii) $d_c \sim 360$ nm; $d_s \sim 43$ nm; $\sigma \sim 5$ nm; NoS ~ 180 (henceforth called NC_D360 nm, corresponds to Figure 2e–h). Note that the TEM images shown in Figure 2a and e are images of the exact same nanoclusters whose scattering spectra are shown. For both NC_D165 nm and NC_D360 nm, the scattering spectra exhibit several well-defined peaks across the 500–1000 nm measurement range. However, the spectra differ in details and magnitude for the polarized excitations employed. Also, the peak positions and intensities are quite different for these two samples. For NC_D165 nm, the spectra associated with azimuthally and radially polarized light (red and green curves, respectively) are weaker (smaller amplitude scattering) than that of linearly polarized light (black curves). We attribute this to the limited spatial overlap of the doughnut-shaped focused vector beams with the nanoclusters (total diameter ~ 225 nm) compared to a Gaussian transverse intensity profile for the linearly polarized beam and the projections of the induced modes back to the detector. In the case of the focused azimuthal CVB, we estimate the diameter of the electric field annulus to be about 600 nm; because of the polarization variation of the beam, the E -field goes to zero at the very center. There is also a notable feature at 900 nm in the linearly polarized spectra that we discuss below.

For NC_D360 nm, the relative intensity of the azimuthal CVB spectrum (red) exceeds that of both the radial CVB (green) and linearly polarized (black) spectra (Figure 2f–h). Moreover, there is a distinct peak between 650 and 700 nm vs the very broad and slightly multi-peaked radial CVB spectrum, which is now more similar to the linearly polarized spectrum. We will discuss specific spectral features below using the corresponding FDTD simulations and multipolar analysis of spectra in the backscattering direction used in the experiments.

Simulations of Nanocluster Scattering Spectra. We performed extensive electrodynamics simulations to complement and interpret the experimental results and report the results within our measurement spectral window (500–1000 nm). The simulation results shown in Figure 2 (dashed curves) were performed with the same number of AgNPs (assumed spherical) and core diameters as were determined in the corresponding TEM images (Figure 2a and e) as described in the text above. Simulations were performed with the FDTD method,³⁶ using a freely available software package MEEP.³⁷ The total field-scattered field method was employed to obtain the scattering spectra. Figure 2 shows that the experimental and simulated scattering spectra of the nanoclusters exhibit very similar characteristics with the appearance of several well-defined peaks across the entire visible–NIR spectrum for the different light excitation polarization conditions. Achieving this required performing FDTD simulations with the correct

number and number density of AgNPs, reasonable distributions of inter-NP distances, and also matching the angular distribution of the electromagnetic scattering to what was done in the experiments. The simulated nanoclusters were built by random packing assuming a 2 nm minimal separation. The SI provides more details and also associated results for other interparticle-limiting separations, including overlapping particles. Importantly, the spectra presented are for a back-scattering geometry with a specific angular range that closely corresponds to our actual experimental setup and numerical aperture of the objective.

However, despite the care taken, there are still differences with the experimental results: (i) the widths of the experimental peaks are often broader; and (ii) the peak positions are somewhat shifted. We attribute these differences to inhomogeneities in size, shape, and distribution of the nanoparticles with some of the Ag nanoparticles touching each other (by contrast, a separation ≥ 2 nm was set in simulation; see SI). Also, the azimuthal and radial states of the experimentally generated cylindrical vector beams are not as perfect as the simulated fields with some scalar beam contamination (perhaps 5%), which can affect the spectra actually obtained. Moreover, as shown in the SI (Figure S4), the details of the spectra can change even just with a permutation of the AgNP arrangements even at constant AgNP number on the same core. Therefore, complete agreement is impossible to achieve for such complex structures. Nevertheless, many similarities do emerge that form the basis of a quantitative analysis.

Assignment of Electric and Magnetic Multipole Features. Understanding the spectral features excited by different types of polarized light requires that we can assign an identity to them. To do this, we perform a near to far field transformation of the total scattering amplitude and then decompose the amplitude into their electric and magnetic multipolar (dipolar, quadrupolar, octupolar) contributions (a detailed description of the procedure is described in Methods). We obtain the dipolar and higher order electric and magnetic modes that give rise to the total scattering (shown in Figure 3) for both NC_D165 nm (Figure 3a–c) and NC_D360 nm (Figure 3d–f) for the three different polarized beams in a backscattering detection geometry for an angular range defined by the experiment. It is well-known that the Ag nanoparticles exhibit pronounced Mie resonances; only the electric dipolar mode is excited for single 40 nm diameter AgNPs.³⁸ However, our FDTD simulations of single SiO₂–Ag core–satellite nanoclusters allow the following assignments: (i) both electric and magnetic modes are excited with linearly polarized light, (Figure 3a and d), hence the scattering spectra obtained are due to excitation of both the electric and the magnetic modes; (ii) azimuthally polarized light exclusively excites (and scatters from) magnetic dipolar, quadrupolar, and octupolar magnetic modes (Figure 3b and e); and (iii) radially polarized light exclusively excites (and scatters from) electric modes (Figure 3c and f). Also, the dominant modes for $d_c = 165$ nm are dipolar and quadrupolar (Figure 3a–c), whereas the dominant modes for $d_c = 360$ nm are quadrupolar and octupolar (Figure 3d–f) at visible–NIR wavelengths. The relative strengths of the electric and magnetic modes for the three different polarizations are shown in Figures S5 and S6.

To compare the experimental scattering spectra from the core–satellite nanoclusters to the FDTD simulated results, we also assign electric/magnetic modes of experimental spectra by using simulated multipolar modes as a set of “basis functions”.

Expanding the experimental spectra in terms of overlap integrals with the multipoles as a basis highlights the character of the vector beam scattering from the nanoclusters. Finally, the overlap between the experimental spectra and each of the multipole expansions was then calculated (see more details in SI and Figure S7). Figure 4 shows the multipolar modes for

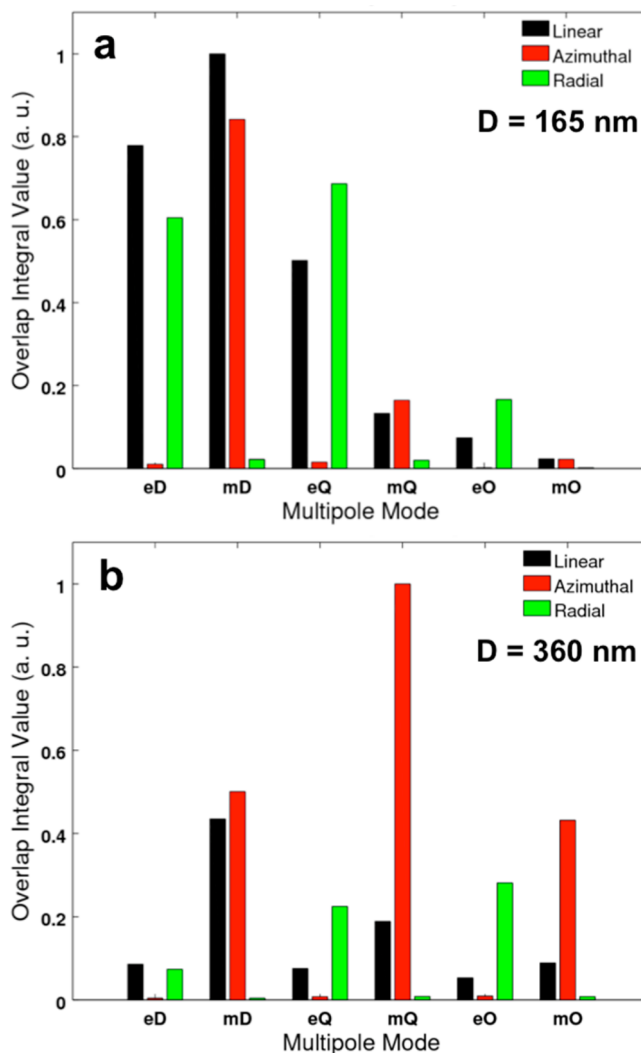


Figure 4. Assignment of experimental multipolar mode content. We use the multipolar expansion analysis in Figure 3 to determine basis functions and overlap integrals with experimental spectra. (a) $D = 165$ nm and (b) $= 360$ nm. The modes excited by the azimuthal CVB are exclusively magnetic in nature, whereas the excitations by the radial CVB are exclusively electric modes. Excitation with focused linearly polarized light gives both. The larger nanocluster shows much more higher order multipolar mode content than the smaller one.

each polarization shown in Figure 2 for each nanocluster. We found the analysis of experimental spectra reached the same conclusion as simulated multipole expansion. That is, while linearly polarized beam excites both electric and magnetic modes, the azimuthally polarized beam can selectively excite magnetic multipolar modes and radially polarized CVB selectively excites electric multipolar modes.

It is also possible to determine the current density and electric displacement current excited in the core–satellite structure from simulation. A visualization of these currents for a $d_c = 360$ nm core–satellite structure and incident azimuthal

beam of wavelength 700 nm is shown in Video S1. The excited mode is a global oscillation of electric displacement current around the Ag NP ring. Therefore, we conclude that our experimental spectra result from selective excitations in the nanoclusters for specific polarization states of the incident beams; magnetic and electric modes for azimuthally and radially polarized CVBs, respectively, and mixtures thereof when using linearly polarized scalar beams. Specifically, the main peak with the azimuthally polarized excitation of Figure 2g is the magnetic quadrupole, with magnetic dipole excitation on the longer wavelength side and magnetic octupole on the shorter wavelength side.

The peak at ~ 900 nm observed in the linearly polarized experimental spectra is not observed in the simulations. We performed many simulations under various conditions of particle density and interparticle separation, but because the FDTD grid cell we use is 1 or 2 nm, we kept a constraint of 2 nm interparticle separation—we did not consider smaller gaps because the grid size is too large to be certain of converged results. However, the TEM images of the nanoclusters (Figure 2) show that short “chains” of Ag nanoparticles with subnanometer gaps are formed. To understand the possible spectral ramifications, we performed FDTD simulations with small grid spacing of short AgNP chains by linearly polarized excitation along the chain axis.

To use finer grids, we performed the simulations with Lumerical (FDTD Solutions). We simulated chains with 2–4 AgNPs, and for each chain the gaps/grid sizes were set between 1.0 and 0.4 nm. The results are shown in Figure S8. The resonances red-shift when the number of AgNPs was increased or the gaps between AgNPs were decreased. Generally the plasmonic resonances of the short chains are in the region of 700–900 nm. One can expect more red-shift (over 900 nm) if there are more AgNPs in the chain (>4), or smaller gaps between AgNPs. These results suggest that the broad peak at 900 nm region is due to short chains of AgNPs. This interpretation is further supported by considering the effect of particle density on the experimental spectra. Figure S9 shows a TEM image and the associated spectra of a nanocluster with reduced AgNP density (vs those shown in Figure 2) that exhibits virtually no peak at ~ 900 nm. Moreover, strong long wavelength (~ 900 – 1200 nm) peaks have been observed in experiment and from other simulations for touching metal nanoparticles.^{39,40}

Most interestingly, the ~ 900 nm peak is not present in the spectra obtained with CVBs since the modes these create are either perpendicularly polarized to the interparticle direction (radial CVB) or involve a collective excitation circumscribing (a large portion of) the circumference of the entire core–satellite cluster to create a magnetic excitation (azimuthal CVB). Therefore, we ascribe the 900 nm peak to short chains of AgNPs of somewhat anisotropic shape.

Position-Dependent Nanocluster Spectra Shifted Away from the Azimuthal Beam Axis and Focal Plane.

Breaking the cylindrical symmetry of the vector beam/nanocluster system (interaction) should result in changes in the measured spectra. For example, if the sample only interacts with an arc of the focused azimuthal beam, one can envision that the excitation becomes more like that obtained with linearly polarized light; one loses the efficient excitation of the full curl of the CVB. Therefore, we measured the scattering spectra of the same nanocluster (NC_D360 nm) as shown in Figure 2e using azimuthally polarized light but with small shifts

of the nanocluster along the y - or z -directions with respect to the beam axis. The results are shown in Figure 5a and b,

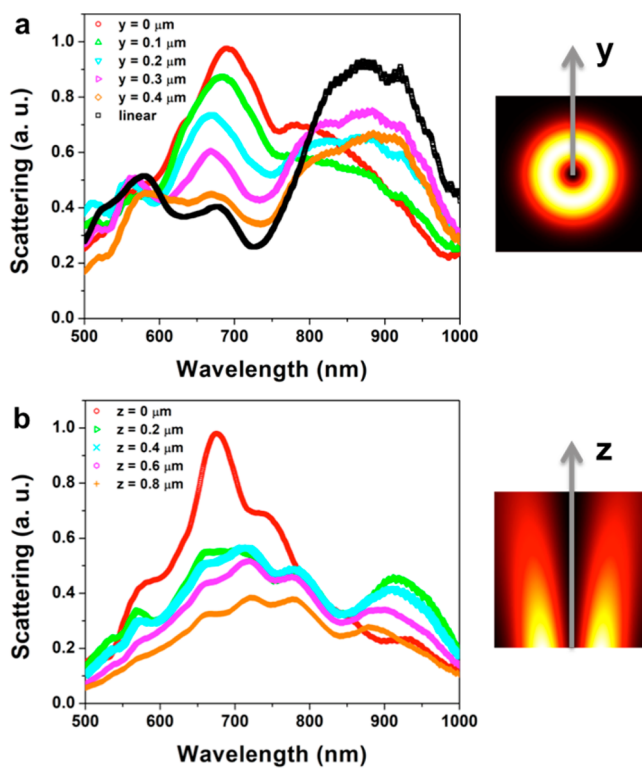


Figure 5. Nanocluster spectra at different y - and z -positions with respect to the beam axis and focal plane. Scattering spectra (colors) for azimuthal polarization while moving the nanocluster in the y - (a) and z - (b) directions. The black spectrum in panel a is the spectrum obtained for linearly polarized light for the same nanocluster. The right panels schematically indicate the directions of the spatial shifts along the y - and z -directions superimposed on appropriate cross sections of E^2 .

respectively. Figure 5a shows that as the nanocluster is moved transversely (along the y -direction), the main peak (at ~ 700 nm) decreases (colored spectra) and finally becomes very similar to the spectrum obtained with linearly polarized light excitation (black). As discussed in Figure 3, the spectrum excited by azimuthally polarized light is the superposition of magnetic multipolar modes (dipole, quadrupole, and octupole). The change of the spectra with increasing y -axis shift corresponds to a decrease of the magnetic mode content and an increase of the electric mode content. Also, the feature at ~ 900 nm also becomes more intense. Therefore, the collective excitations (i.e., longitudinal loops) around the core–satellite clusters are required for magnetic mode excitation.

Figure 5b shows a decrease in the magnitude and some changes in the spectral shape of the scattering spectra when moving the beam away from the focal plane (along the axial or z -direction). The decreasing scattering with shift from the focus can be understood as a decrease of spatial overlap of the expanding beam with the nanocluster. However, the changing spectral shape suggests that more is occurring. Indeed as shown in the inset to Figure 5b, the magnetic character of the focused azimuthal CVB, which has a maximal longitudinal amplitude and is most concentrated at the focus, diminishes with increasing shift from the focal plane.^{27,33} There is a progressive diminishment of this spatial segregation and its longitudinal

polarization as one moves away from the focal plane so that the electric and magnetic field distributions of the beam are the same in the far field. Moreover, this focused magnetic field interferes with the magnetic field that arises from the electronic displacement current and the concomitant induction of the magnetic mode. The longitudinally polarized magnetic field of the focused azimuthal CVB can therefore enhance or diminish the degree of excitation of the magnetic mode in the nanocluster by its relative phase and amplitude. This amplitude diminishes rapidly away from the focal plane.²⁷

Conclusion. Electromagnetic responses that are studied at optical frequencies are almost always electric dipolar (or quadrupolar) since magnetic-dipole transitions at optical frequencies have approximately 10^5 times smaller absorption cross sections than electric dipole transitions⁶ with the exception of the rare earth elements^{7,8} and engineered metamaterials.^{12–15,18,24,41} Here, we have demonstrated that optical vector beams can be used to selectively drive magnetic multipole excitations in metal-based nanostructures and that these excitations can be stronger than the electric multipolar modes of the identical structures. The magnetic modes can be understood as a collective excitation of electrodynamically coupled metal nanoparticles excited by a time varying azimuthally polarized electric field with instantaneous curl. The displacement currents produced in association with the azimuthal polarization induce a magnetic field analogous to that created by induction due to circulating electric currents in electromagnets.

The magnetic modes excited by azimuthally polarized CVBs and with linearly polarized light are different in both the near- and far-fields. In the far-field the modes are in perpendicular orientations; with azimuthal CVBs the magnetic modes are always oriented along the beam propagation direction (e.g., z -axis polarized). More importantly, the mechanism by which each beam excites the magnetic modes is different. A z -oriented magnetic dipole mode is created by exciting an effective displacement current in the xy -plane due to the unique nature of the azimuthally polarized beam's polarization state and the coupled particle dipoles. A linearly x -polarized beam excites a y -oriented magnetic dipole mode by exciting an effective displacement current in the xz -plane. A current density in the z -direction is made possible by retardation of the beam along the z -axis, while a current density in the x -direction occurs due to the polarization of the beam. Combined, these effects yield an effective current in the xz -plane. This behavior is seen in Figure S10 in the SI: displacement currents circulate in different planes for each beam.

Conventional induction of magnetic (dipole) modes in nano-meso scale metamaterials relies upon the design of the structure. In contrast, our work shows that one can control the nature of the excitation with the optical field as well. Since we obtain the curl (or instantaneous angular momentum) from a focused azimuthal CVB, one should be able to drive a magnetic response in metal nanoparticle based materials that do not have morphology with cylindrical symmetry. In other words, a “beam engineering”¹⁰ approach should allow inducing optical magnetism in “arbitrary” metal nanoparticle based structures that can support the creation of displacement currents on the scale of the focused CVB (e.g., monolayer films of nanoparticles). We are currently investigating this possibility.

Methods. Materials and Instruments. Silver nitrate (AgNO_3 , >99.8%) was purchased from MP Biomedicals, LLC. Tannic acid was obtained from Alfa Aesar. Trisodium

citrate dihydrate (>99.5%, BioUltra, for molecular biology), N -(3-(dimethylamino)propyl)- N' -ethylcarbodiimide hydrochloride (EDC, BioXtra), N -hydroxysulfosuccinimide sodium salt (NHS, >98%, HPLC), 3-mercaptopropionic acid (MPA, >99.0%, HPLC), and polyethylene glycol sorbitan monolaurate (Tween 20, molecular biology, viscous liquid) were purchased from Sigma-Aldrich. Amine-functionalized silica nanoparticles (300 and 150 nm, 50 mg/mL) were acquired from Kisker Biotech GmbH & Co. KG. All chemicals were purchased from commercial suppliers and used without further purification. Nanopure water (18.2 M Ω , Barnstead Nanopure, Thermo Scientific, MA, USA) was used in all experiments. RCT basic and heating block (IKA, NC, US) was used for magnetic stirring and heating. Ultraviolet–vis spectra were measured with Synergy H4 (Biotek, VT, USA). The Formvar/carbon-coated copper grid (Ted Pella, Inc. Redding, CA, USA) and transmission electron microscopy (Tecnaï G2 Spirit, 120 kV, FEI, OR, USA) were used for the TEM analysis. Scanning electron microscopes (MERLIN, Carl Zeiss, Oberkochen, Germany) were used for the SEM analysis. SEM images were obtained at the accelerating voltage of 3 kV.

Synthesis of Core (SiO_2)–Satellite (AgNPs) Nanoclusters. The silver nanoparticle seed solution was synthesized by a modified literature procedure.³⁴ Briefly, the silver seeds were prepared with 80 mL of ultrapure water, 10 mL of 1 mM tannic acid, and 10 mL of 50 mM sodium citrate. The mixture, contained in a three-neck round-bottomed flask, was heated with a heating block under vigorous magnetic stirring. A condenser was used to prevent evaporation. Once the temperature reached 100 °C, 1 mL of 25 mM AgNO_3 was quickly injected into the boiling mixture, which was then kept at 100 °C for 20 min.

To dilute the seed solution, 19.5 mL of the seed solution was extracted, and then 16.5 mL of ultrapure water was added. Then, the temperature was lowered to 90 °C, and 0.5 mL of 25 mM sodium citrate, 1.5 mL of 2.5 mM tannic acid, and 1 mL of 25 mM AgNO_3 were added sequentially under vigorous magnetic stirring. The solution was kept at 90 °C for 20 min, and an aliquot of 0.1 mL was extracted for characterization to confirm the size of the particles. This regrowth process was repeated to get the desired size of nanoparticles. The resulting solution was centrifuged at 13 000 g for 20 min at room temperature and washed with 2.2 mM of sodium citrate, repeated twice. Finally, the pellet of silver nanoparticles was redispersed in 25 mL of 2.2 mM of sodium citrate for the next step.

For the thiolation of amine-functionalized silica nanoparticles, 62.5 μL of 32 mM EDC and 62.5 μL of 80 mM NHS in 0.1 M 2-(N -morpholino) ethanesulfonic acid buffer (MES, 0.9% NaCl, pH 5.01) were added twice in 15 min intervals to 250 μL of 0.8 mM MPA in 0.1 M MES buffer (0.9% NaCl, pH 5.01) and kept at room temperature under vigorous vortexing. After 30 min, the pH of the solution was adjusted to 7.2–7.4 by adding 500 μL of 1 M phosphate-buffered saline buffer (PBS, 0.15 M NaCl, pH 7.32). Finally, 20 μL of amine-functionalized silica nanoparticles (300 or 150 nm, 50 mg/mL) was added and kept for 2 h at room temperature under vigorous vortexing. The resulting solution was centrifuged at 2000 g for 5 min and washed with 1 mL of 0.01% Tween-20 in ultrapure water, repeated twice, then redispersed in 20 μL of 0.01% Tween 20 in ultrapure water for the next step.

For the synthesis of core (SiO_2)–satellite (AgNPs) nanoclusters, 5 mL of the prepared silver nanoparticle solution was

centrifuged at 12 000 g for 15 min at room temperature, then redispersed in 90 μL of 10 mM sodium citrate buffer (pH 3.5, 0.01% tween 20). Ten μL of thiolated silica nanoparticles (300 or 150 nm, 50 mg/mL) was quickly mixed with 90 μL of concentrated silver nanoparticles in 1.5 mL centrifuge tube and kept overnight at 1500 rpm at room temperature using vortex mixer (Fisher Scientific). The resulting solution was diluted by adding 950 μL of 0.01% Tween-20 in ultrapure water. The diluted solution was centrifuged at 500–1000 g for 8 min and washed with 1 mL of 0.01% Tween-20 in ultrapure water, repeated until free silver nanoparticles are removed from the solution, then redispersed in 0.01% Tween-20 in ultrapure water for further characterization. The ensemble UV–vis spectra and their associated TEM images for nanoclusters are shown in Figure S2.

Measurements of Scattering Spectra of Core–Satellite Structures. The scattering spectra were measured using a home-built microscopy setup. A schematic of the vector beam spectroscopy setup is shown in Figure S1b. A spatially coherent (broadband) white light continuum (Fianium, White Lase SC400, from 400 to 1000 nm) was coupled to an inverted optical microscope equipped with an oil immersion objective with numerical aperture, $\text{NA} \leq 1.4$ (Olympus, IX-81; SAPO 100X). The vector beam generator was placed just before the microscope objective and positioned using a translation stage. The backscattered images and spectra of the sample plane were recorded either by a CCD array detector (Andor, sCMOS) connected to the eyepiece of the microscope or by a CCD (Andor, Newton) connected to an imaging spectrometer (Shamrock 193i) coupled to the side port of the microscope via a home-built achromatic $4f$ relay system. The aqueous dispersion of nanoclusters was dropcasted on a Formvar coated TEM finder grid. After drying, TEM images were acquired before taking scattering spectra. Figure S3 shows the same area of the grid imaged by TEM and the optical microscope. Thus, we can do single particle spectroscopy, which can obtain the structure and scattering spectra on individual nanoclusters. The grid was sandwiched by two glass slides and embedded in immersion oil. Thus, the refractive index of the space between the coverslip and grid is nearly perfectly matched, and the scattering from the oil/Formvar interface is very weak.

The vector beam generator used here is a liquid-crystal based polarization converter (ARCOptix, Switzerland), which can generate azimuthally and radially polarized cylindrical vector beams.³² To obtain a fully azimuthal or radial beam, there is a phase compensator in vector beam generator, which permits compensation of the $\lambda/2$ phase step between the upper and lower halves of the polarization converter (theta-cell). The phase compensation depends on the voltage applied to the phase compensator. By changing the voltage, the optimized wavelength band shifted. Thus, broadband measurements at one fixed voltage cannot be performed over the whole band (500–1000 nm). Rather, we calibrated the relation between voltage and the corresponding wavelength range, in which a high quality vector beam, that is, a nice doughnut shape, is observed. To cover the whole spectra range (400–1000 nm), we measured six spectra with different voltages for an individual nanocluster. In post processing data analysis, we “stitched” these spectra according to the voltage–wavelength relation. Specifically, we took each of the spectra and multiply it by a Gaussian weight function, centered at the optimal wavelength designated by the voltage with a width of 100 nm, and then stitched the weighted spectra together. Since the noise is very

strong in the range of 400–500 nm, the features could not be well-observed in the measurements, so we cut the experimental spectra at 500 nm.

Simulations of Scattering Spectra from Core–Satellite Structures. Simulations were performed with the FDTD method,³⁶ using a freely available software package MEEP.³⁷ The core (SiO_2) was modeled as a dielectric of index 1.46. A background index of 1.50 (oil) was used. Silver nanoparticles were placed randomly on the surface of sphere, with a restriction that the minimum separation between any two spheres was 2 nm. The dielectric function of silver was chosen as a Drude–Lorentz model to fit the Johnson–Christy dielectric function measurements of silver.⁴² The incident source carried a polarization state (linear, radial, or azimuthal) and a Gaussian envelope (spatially and temporally). A spatial Gaussian envelope was chosen to give the beam a 300 nm diameter. The temporal Gaussian envelope was chosen to span the incident wavelengths from 400–1000 nm. A perfectly matched layer (PML) was used at the boundary to model radiation leaving the simulation domain. The simulation was then time-stepped until the fields decayed and the scattering spectra converged. Figure S11 shows a diagram of the simulation box.

The electric fields were collected on the surface of a spherical monitor surrounding the core–satellite structure. As a postprocessing step, these fields were used to compute a multipole expansion of the scattered radiation, using eqs 1 and 2.^{43–45}

$$a_{nm} = \frac{\int_0^{2\pi} \int_0^\pi \mathbf{E}_{\text{scat}} \cdot \mathbf{N}_{nm}^* \sin \theta \, d\theta \, d\phi}{\int_0^{2\pi} \int_0^\pi |\mathbf{N}_{nm}|^2 \sin \theta \, d\theta \, d\phi} \quad (1)$$

$$b_{nm} = \frac{\int_0^{2\pi} \int_0^\pi \mathbf{E}_{\text{scat}} \cdot \mathbf{M}_{nm}^* \sin \theta \, d\theta \, d\phi}{\int_0^{2\pi} \int_0^\pi |\mathbf{M}_{nm}|^2 \sin \theta \, d\theta \, d\phi} \quad (2)$$

Here, a_{nm} and b_{nm} are the electric and magnetic multipole coefficients, respectively, of order n and spherical orientation m . Physically, $n = 1$ are the dipole modes, $n = 2$ are the quadrupole modes, and so forth, and $m = -n, -n + 1, \dots, 0, \dots, n - 1, n$ specifies different orientations of the mode. The complex vector fields \mathbf{N}_{nm} and \mathbf{M}_{nm} are the vector spherical harmonics.

The scattering intensity is then computed using eq 3,

$$C_{\text{sca}} = k^2 \sum_{n=1}^{\infty} \sum_{m=-n}^n n(n+1) (|a_{nm}|^2 + |b_{nm}|^2) \quad (3)$$

Here, k is the wavenumber of the incident radiation. Each term in the sum represents the scattering intensity of a particular electric or magnetic mode.

This method was used for radiation up to octupole order for both electric and magnetic modes. Figure 4 shows the multipole expansion results for two different core–satellite structures. Equations 1 and 2 also allow the fields to be projected into the far-field, from which angular scattering quantities can be computed. To determine spectra in the back scattering direction to mimic the experiments, the far-field Poynting vector is integrated over the cap of a cone with apex angle 140° , oriented in the backward direction. Figure 3 shows simulated back scattering spectra in comparison with experiment.

Additional simulations were done to investigate the role of a glass–water interface. A core–satellite structure in a water medium was placed on a glass substrate. The glass–water interface introduces additional scattering and has a notable impact on the back scattering intensity (see Figure S12). For this reason, an oil medium was used to nearly index match the oil–substrate interface and reduce the unwanted reflections in experiment.

■ ASSOCIATED CONTENT

● Supporting Information

The Supporting Information is available free of charge on the ACS Publications website at DOI: 10.1021/acs.nanolett.7b02144.

Details of the vector beam spectroscopy setup; ensemble UV–vis spectra and TEM images of nanoclusters; TEM and optical microscopy images of EM finder grid; FDTD simulated spectra of 360 nm diameter nanocluster with three different permutations of AgNPs on surface of SiO₂ core; multipole expansion spectra of nanoclusters; details of multipole expansion analysis of experimental data; FDTD simulations of short chains of AgNPs; spectra of low surface density nanoclusters; the simulation setup (PDF)

Video of the current density and displacement current as a function of time (ZIP)

■ AUTHOR INFORMATION

Corresponding Author

*E-mail: nfschere@uchicago.edu.

ORCID

Tian-Song Deng: 0000-0002-0841-4932

Yossi Weizmann: 0000-0002-3467-990X

Present Address

U.M.: Department of Physics, Illinois State University, Normal, Illinois 61790, United States.

Author Contributions

[§]U.M., J.-H.L., T.-S.D., and J.P. contributed equally to this work. N.F.S., Y.W., and U.M. designed the research; U.M. installed the set-ups; T.S.D. and U.M. performed the measurements; J.H.L. and Y.W. synthesized the nanocluster samples; J.P. performed the simulations; N.S. helped in installing set-ups and performing measurements; T.S.D., J.P., N.S., and U.M. analyzed the data; U.M., T.S.D., Y.W., and N.F.S. wrote the manuscript; Y.W. and N.F.S. supervised the project; and all authors discussed the results and commented on the manuscript.

Notes

The authors declare no competing financial interest.

■ ACKNOWLEDGMENTS

We thank Dr. Stephen K. Gray for helpful conversations on electrodynamic simulations and analysis. We thank Dr. Yuval Yifat for performing FDTD simulations of short AgNP chains. The authors acknowledge support from the Vannevar Bush Faculty Fellowship program sponsored by the Basic Research Office of the Assistant Secretary of Defense for Research and Engineering and funded by the Office of Naval Research through grant N00014-16-1-2502. We also acknowledge the University of Chicago NSF MRSEC for central facilities use. We also thank the University of Chicago Research Computing

Center for a grant of computer time for the FDTD simulations reported here. The simulations using Lumerical were performed at the Center for Nanoscale Materials, a U.S. Department of Energy Office of Science User Facility, and supported by the U.S. Department of Energy, Office of Science, under Contract No. DE-AC02-06CH11357.

■ REFERENCES

- (1) Maxwell, J. C. *Philosophical Transactions of the Royal Society of London* **1865**, 155, 459–512.
- (2) Bloch, F.; Hansen, W. W.; Packard, M. *Phys. Rev.* **1946**, 69, 127–127.
- (3) Purcell, E. M.; Torrey, H. C.; Pound, R. V. *Phys. Rev.* **1946**, 69, 37–38.
- (4) Slichter, C. P. *Principles of Magnetic Resonance*; Springer, 1990.
- (5) Zavoisky, E. J. *Phys. USSR* **1945**, 9, 211–216.
- (6) Cowan, R. D. *The Theory of Atomic Structure and Spectra*; University of California Press: Berkeley, CA, 1981.
- (7) Taminiau, T. H.; Karaveli, S.; van Hulst, N. F.; Zia, R. *Nat. Commun.* **2012**, 3, 979.
- (8) Kasperczyk, M.; Person, S.; Ananias, D.; Carlos, L. D.; Novotny, L. *Phys. Rev. Lett.* **2015**, 114, 163903.
- (9) Miroshnichenko, A. E.; Liu, W.; Neshev, D.; Kivshar, Y. S.; Kuznetsov, A. I.; Fu, Y. H.; Luk'yanchuk, B. *Opt. Photonics News* **2012**, 23, 35.
- (10) Das, T.; Iyer, P. P.; DeCrescent, R. A.; Schuller, J. A. *Phys. Rev. B: Condens. Matter Mater. Phys.* **2015**, 92, 241110.
- (11) Das, T.; Schuller, J. A. *Phys. Rev. B: Condens. Matter Mater. Phys.* **2017**, 95, 201111.
- (12) Pendry, J. B.; Holden, A. J.; Robbins, D. J.; Stewart, W. J. *IEEE Trans. Microwave Theory Tech.* **1999**, 47, 2075–2084.
- (13) Shelby, R. A.; Smith, D. R.; Schultz, S. *Science* **2001**, 292, 77–79.
- (14) Veselago, V. G. *Soviet Physics USPEKHI-USSR* **1968**, 10, 509–514.
- (15) Alù, A.; Salandrino, A.; Engheta, N. *Opt. Express* **2006**, 14, 1557–1567.
- (16) Fruhnert, M.; Mühligh, S.; Lederer, F.; Rockstuhl, C. *Phys. Rev. B: Condens. Matter Mater. Phys.* **2014**, 89, 075408.
- (17) Li, J.; Engheta, N. *Phys. Rev. B: Condens. Matter Mater. Phys.* **2006**, 74, 115125.
- (18) Simovski, C. R.; Tretyakov, S. A. *Phys. Rev. B: Condens. Matter Mater. Phys.* **2009**, 79, 045111.
- (19) Jiang, R. B.; Li, B. X.; Fang, C. H.; Wang, J. F. *Adv. Mater.* **2014**, 26 (31), 5274–5309.
- (20) Liu, W.; Miroshnichenko, A. E.; Neshev, D. N.; Kivshar, Y. S. *ACS Nano* **2012**, 6 (6), 5489–5497.
- (21) Chen, H. J.; Shao, L.; Man, Y. C.; Zhao, C. M.; Wang, J. F.; Yang, B. C. *Small* **2012**, 8 (10), 1503–1509.
- (22) Gong, B. Y.; Zhao, X. P.; Pan, Z. Z.; Li, S.; Wang, X. N.; Zhao, Y.; Luo, C. R. *Sci. Rep.* **2015**, 4, 4713.
- (23) Qian, Z. X.; Hastings, S. P.; Li, C.; Edward, B.; McGinn, C. K.; Engheta, N.; Fakhraei, Z.; Park, S. J. *ACS Nano* **2015**, 9 (2), 1263–1270.
- (24) Sheikholeslami, S. N.; Alaeian, H.; Koh, A. L.; Dionne, J. A. *Nano Lett.* **2013**, 13 (9), 4137–4141.
- (25) Hall, D. G. *Opt. Lett.* **1996**, 21 (1), 9–11.
- (26) Greene, P. L.; Hall, D. G. *J. Opt. Soc. Am. A* **1996**, 13 (5), 962–966.
- (27) Novotny, L.; Hecht, B. *Principles of Nano-Optics*; Cambridge University Press, 2006.
- (28) Youngworth, K. S.; Brown, T. G. *Proc. SPIE* **2000**, 3919, 75–85.
- (29) Zhan, Q. W. *Adv. Opt. Photonics* **2009**, 1 (1), 1–57.
- (30) Dorn, R.; Quabis, S.; Leuchs, G. *Phys. Rev. Lett.* **2003**, 91 (23), 233901.
- (31) Toussaint, K. C.; Park, S.; Jureller, J. E.; Scherer, N. F. *Opt. Lett.* **2005**, 30 (21), 2846–2848.
- (32) Stalder, M.; Schadt, M. *Opt. Lett.* **1996**, 21 (23), 1948–1950.

- (33) Youngworth, K. S.; Brown, T. G. *Opt. Express* **2000**, *7* (2), 77–87.
- (34) Bastus, N. G.; Merkoci, F.; Piella, J.; Puntès, V. *Chem. Mater.* **2014**, *26* (9), 2836–2846.
- (35) Love, J. C.; Estroff, L. A.; Kriebel, J. K.; Nuzzo, R. G.; Whitesides, G. M. *Chem. Rev.* **2005**, *105*, 1103–1169.
- (36) Taflová, A.; Hagness, S. C. *Computational Electrodynamics: The Finite-Difference Time-Domain Method*; Artech House: Boston, 2004.
- (37) Oskooi, A. F.; Roundy, D.; Ibanescu, M.; Bermel, P.; Joannopoulos, J. D.; Johnson, S. G. *Comput. Phys. Commun.* **2010**, *181* (3), 687–702.
- (38) Tamaru, H.; Kuwata, H.; Miyazaki, H. T.; Miyano, K. *Appl. Phys. Lett.* **2002**, *80* (10), 1826–1828.
- (39) Herrmann, L. O.; Valev, V. K.; Tserkezis, C.; Barnard, J. S.; Kasper, S.; Scherman, O. A.; Aizpurua, J.; Baumberg, J. J. *Nat. Commun.* **2014**, *5*, 6.
- (40) Romero, I.; Aizpurua, J.; Bryant, G. W.; de Abajo, F. J. G. *Opt. Express* **2006**, *14* (21), 9988–9999.
- (41) Burreli, M.; van Oosten, D.; Kampfrath, T.; Schoenmaker, H.; Heideman, R.; Leinse, A.; Kuipers, L. *Science* **2009**, *326* (5952), 550–553.
- (42) Johnson, P. B.; Christy, R. W. Optical constants of noble metals. *Phys. Rev. B* **1972**, *6*, 4370–4379.
- (43) Grahn, P.; Shevchenko, A.; Kaivola, M. *New J. Phys.* **2012**, *14*, 11.
- (44) Mühligh, S.; Menzel, C.; Rockstuhl, C.; Lederer, F. *Metamaterials* **2011**, *5*, 64–73.
- (45) Parker, J.; Gray, S.; Scherer, N. F. Multipolar analysis of electric and magnetic modes excited by vector beams in core-satellite nanostructures. *arxiv: 1711.06833*, **2017**.